ORNL/TM-2024/3292

Nanostructured Alumina Forming Austenitic Alloy (NAFA) Production Using Mechanical Alloying and High-Temperature Consolidation

Tim Graening
Caleb Massey
David Hoelzer
Yukinori Yamamoto
Sebastien Dryepondt
Holden Hyer
Selda Nayir
Josh Kendall

March 2024

M3FT-24OR060101032

OAK RIDGE National Laboratory

ORNL IS MANAGED BY UT-BATTELLE LLC FOR THE US DEPARTMENT OF ENERGY

ORNL/TM-2024/3292

Innovative Nuclear Materials Program

NANOSTRUCTURED ALUMINA FORMING AUSTENITIC ALLOY (NAFA) PRODUCTION USING MECHANICAL ALLOYING AND HIGH-TEMPERATURE CONSOLIDATION

Tim Graening
Caleb Massey
David Hoelzer
Yukinori Yamamoto
Sebastien Dryepondt
Holden Hyer
Selda Nayir
Josh Kendall

March 2023

M3FT-24OR060101032

Prepared by
OAK RIDGE NATIONAL LABORATORY
Oak Ridge, TN 37831
managed by
UT-BATTELLE LLC
for the
US DEPARTMENT OF ENERGY
under contract DE-AC05-00OR22725

CONTENTS

LIST OF FIGURES

LIST OF TABLES

Table 1. Specified chemical compositions of gas-atomized AFA alloy powder used in this work. The compositions are in weight percent, as provided in supplier material certifications. 3
Table 2. Specified chemical compositions of INM-specific gas-atomized AFA powder used for future work. 13

ABBREVIATIONS

AFA	alumina-forming austenitic
BB	Bragg–Brentano
BF	bright field
EDS	energy dispersive x-ray spectroscopy
EBSD	electron backscatter diffraction
FIB	focused ion beam
GARS	gas atomization reaction synthesis
HIP	hot isostatic pressing
HTHE	high-temperature helium embrittlement
ICSD	Inorganic Crystal Structure Database
IPF	inverse pole figure
KAM	kernel average misorientation
NAFA	nanostructured AFA
LFR	lead-cooled fast reactor
OD	outer diameter
ODS	oxide dispersion–strengthened
ORNL	Oak Ridge National Laboratory
SEM	scanning electron microscopy
STEM	scanning transmission electron microscopy
TE	total elongation
TEM	transmission electron microscopy
UE	uniform elongation
UTS	ultimate tensile stress
XRD	x-ray diffraction
YS	yield stress

ACKNOWLEDGMENTS

This research was sponsored by the US Department of Energy Office of Nuclear Energy's Innovative Nuclear Materials Program under contract DE-AC05-00OR22725 with UT-Battelle LLC. One of the alloys analyzed in this work was originally developed under the Powertrain Materials Core Program, Vehicle Technologies Office, Office of Energy Efficiency and Renewable Energy. The authors thank Mr. Ben Garrison and Dr. Stephen Taller for their thoughtful review of this report before publication. The authors would also like to thank Daniel Newberry and Jim Horenburg for their assistance with sample preparation. Finally, the research team would like to acknowledge Alex Rogers for his assistance in powder consolidation via hot isostatic pressing, as well as the dedicated team of high-bay personnel (Kevin Hanson, Ryan Dalton, and Cody Taylor) for alloy extrusion services.

ABSTRACT

Alumina-forming austenitic (AFA) alloys are a promising class of nuclear materials because of their high-temperature oxidation/corrosion resistance and mechanical properties. Unfortunately, these alloys are limited in use for core material applications, and they are specifically limited for use as nuclear fuel cladding because of their high Ni-transmutation and helium generation rate in-service. Improving these alloys through a fine dispersion of oxide precipitates and thus increasing the effective irradiation sink strength of the alloy system may mitigate many of the degradation phenomena expected during alloy deployment. These phenomena include high-temperature helium embrittlement and cavity swelling for lead-cooled fast reactor applications. This work effort uses combination of conventional and advanced manufacturing approaches are being used to fabricate nanostructured AFA (NAFA) materials. As the first objective of this initiative, a conventional AFA was modified using mechanical alloying and extrusion to alter the precipitation characteristics to include a fine dispersion of nanoscale oxides intended to serve as traps for irradiation-induced point defects and transmuted He within the lattice. This analysis compared the efficacy of the conventional mechanical alloying and extrusion approach with the unalloyed AFA consolidated approach using hot isostatic pressing (HIP). It was found that, although the mechanical alloying approach is successful in producing a fine distribution of oxides within the first nanostructured AFA (NAFA-1), the distribution is heterogeneous because of the mild milling parameters used to prevent cold welding of powder to the spherical milling media. The additional dispersion of oxides, coupled with a higher volume fraction of other secondary phases in the NAFA-1, produces higher alloy strengths that range up to 600°C in comparison to the unalloyed HIP AFA, thus exceeding the operating temperature of lead-cooled fast reactors. However, the strength of the NAFA-1 is lower than that of the HIP AFA at 800°C, which is presumed to be a function of increased secondary phases from the nonoptimized AFA chemistry. Future work is planned on a newly procured NAFA-2 chemistry that is more suitable for advanced reactor applications exploring new manufacturing routes.

1. INTRODUCTION

Nuclear energy is at a crossroads: many new nuclear reactor concepts require rapid qualification to address the rapidly growing demand for carbon-neutral energy solutions. Unfortunately, many of these concepts, including advanced lead-cooled fast reactors (LFRs) and heat-pipe microreactors, require materials with high creep strength, irradiation resistance, and resistance to oxidation and corrosion in the presence of coolants including air, supercritical CO_2, and liquid lead. Fortunately, alumina-forming austenitic (AFA) stainless steels are a class of fully face-centered cubic (fcc) iron-based alloys designed for use in extreme environments that require oxidation resistance at high temperatures. Originally designed in the early 2000s for use in fossil power generating systems as boiler tubing, steam turbine components, and similar components, this class of alloys was designed with increased levels of aluminum addition to form a passive aluminum oxide scale instead of the chromium oxide scales normally formed on conventional stainless steels [1].

Significant repositories of data on fossil-grade AFA alloys have been produced over the past decade, particularly with reference to oxidation and creep performance, and recently, a subset of these alloys is being considered as a structural material candidate for advanced reactor applications, including in LFRs [2]. Unfortunately, it is yet to be seen whether AFA alloys, which do have a high density of intermetallic and carbide precipitates, depending on their composition, have sufficient sink strength to balance the increased helium generation resulting from the higher nickel content of this alloy system, and postulated increase in cavity swelling.

Irrespective of the final application, AFA alloys in their current wrought form have promise as nuclear structural materials, but practical challenges remain before their implementation as core materials such as fuel cladding) can be realized. One potential approach to increasing AFA relevance to core material applications is to increase the number density of nanoscale features that serve as recombination sites for irradiation-induced defects, , or *sinks*. If the sink strength of this material class can be readily increased, then without degradation of other properties, it may help mitigate concerns such as high-temperature helium embrittlement (HTHE) and/or helium-induced cavity stabilization, in these austenitic alloys, and it may also enable the use of AFAs as a core material in LFRs. If these gains can be realized, then the use of nanostructured alumina forming austenitic (NAFA) alloys would rapidly expand the design space LFRs or microreactors without requiring an additional environmental barrier coating.

The design of high sink strength oxide dispersion–strengthened (ODS) AFA variants is thus pursued in this work package to produce tubes for fuel cladding. A previous report [3] outlined the design strategy, which includes: (a) thermodynamic and neutronic design of AFA alloys with reactor-specific compositions, (b) demonstration of laboratory-scale NAFA alloy production using conventional ODS alloy fabrication technologies, and (c) expansion of the NAFA alloy processing window by using advanced manufacturing, as shown in Figure 1.

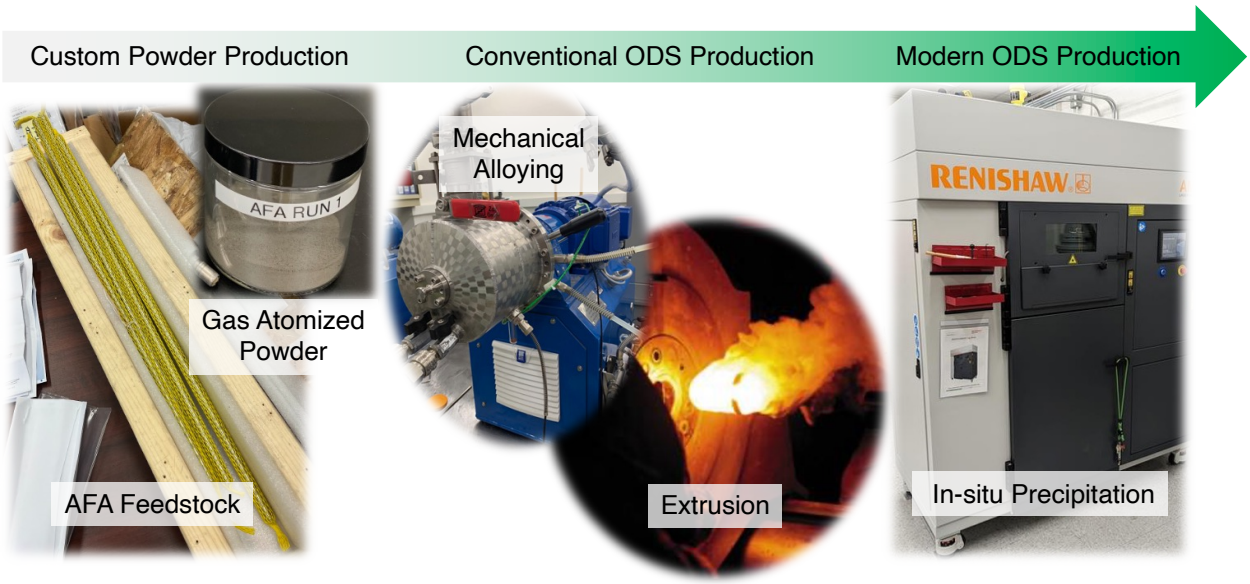

Figure 1. NAFA alloy design strategy implemented in this work package. Following custom powder production, conventional NAFA alloy strategies of mechanical alloying followed by high-temperature consolidation will be used to create a sink strength target as a precursor to modern manufacturing.

2. MATERIALS AND METHODS

2.1 NAFA-1 PRECURSOR POWDER SPECIFICATIONS

The compositional specification and measured composition of the initial powder investigated in this work is presented below in Table 1. These values were provided by the powder supplier, Powder Alloy Corporation, using a combination of inductively coupled plasma mass spectroscopy, inert gas fusion, and combustion analysis. This AFA (VA05) was originally designed for the vehicle technologies program, and powder was already available onsite at Oak Ridge National Laboratory (ORNL) for immediate experimental investigations in FY23. The composition of the alloy, which has high C content and highly reactive minor alloying elements, was designed to maximize the formation of secondary carbide $M_{23}C_6$ as a strengthening phase, with consumption of M_7C_3 forming during the solidification process, thus providing superior high-temperature strength. Optimization of mechanical properties can be achieved by tailored heat treatment to increase the number density of carbide precipitates above the formation temperature of B2-NiAl, which is approximately 900°C, for a short duration to dissolve any formed NiAl while restricting the growth of carbide precipitates. Heat treatment optimization was not part of this milestone and will be addressed in combination with additive manufacturing later this year, with a focus on formation of large number densities of nanoscale precipitates. In this work, conventionally produced NAFA-1 will be examined in as-extruded condition in comparison to the same material, omitting the mechanical alloying step. A phase diagrams for initial (VA05) powder composition used in this work to create NAFA-1 is shown in Figure 2.

Table 1. Specified chemical compositions of gas-atomized AFA alloy powder used in this work. The compositions are in weight percent, as provided in supplier material certifications.

Element	VA05 (used to make NAFA-1)	
	Specification (wt %)	Supplier certification (wt %)
Fe	bal.	bal.
Ni	22.0	23.0
Cr	17.5	17.6
Al	4.0	4.0
Mn	2.0	2.0
Mo	1.0	0.98
W	0.5	0.5
Si	0.5	0.4
Nb	0.7	0.7
Zr	0.10	0.13
Y	0.10	0.10
C	0.50	0.50
B	0.01	0.01
N	<0.05	0.04
O	<0.03	0.02

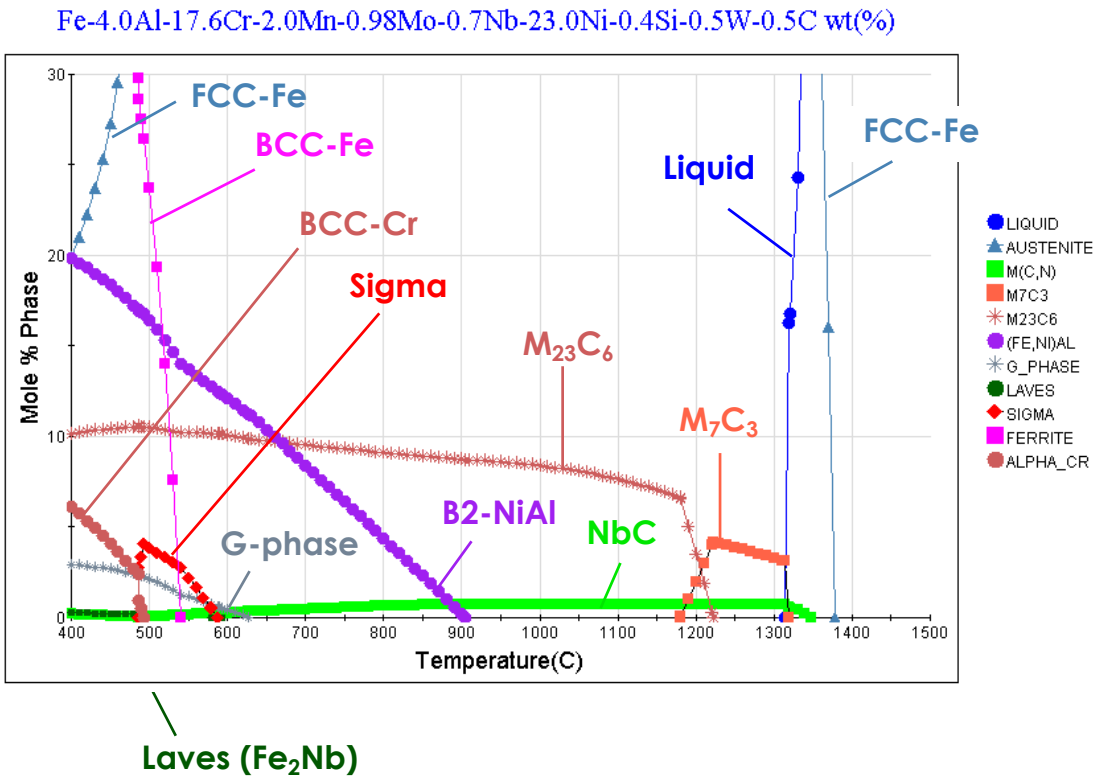

Figure 2. Phase diagrams for initial (VA05) powder composition used in this work to create NAFA-1.

2.2 MECHANICAL ALLOYING AND HIGH-TEMPERATURE CONSOLIDATION

The VA05 AFA powder gas-atomized form sieved to a +270 mesh (< 50 μm) was mechanically alloyed with 0.3% by weight of Y_2O_3 powder in a Zoz Simoloyer attrition ball mill using mild-steel milling media and a ball-to-powder ratio of 10:1. Because of initially low yields (10%) following high rpm mechanical alloying runs, the milling time was reduced to 20 h, and milling speed was reduced to 300 rpm, increasing powder yield to ~60% when milling in Ar atmosphere [3]. Powder was then sent to DIRATS Laboratories for impurity analysis via inert gas fusion and combustion analysis. The resulting chemical analysis given in Figure 3 shows that the ball milling process did not change C or N contents, but it did increase the oxygen content from 200 ppmw to 850 ppmw as a result of the intentional addition of yttria. The values in this figure are only differ marginally from the supplier specifications of the initial gas atomized powder in Table 1. This was not caused by pre-alloy impurities, which are often seen when using elemental powders, but was instead caused by oxygen pickup during the mechanical alloying process.

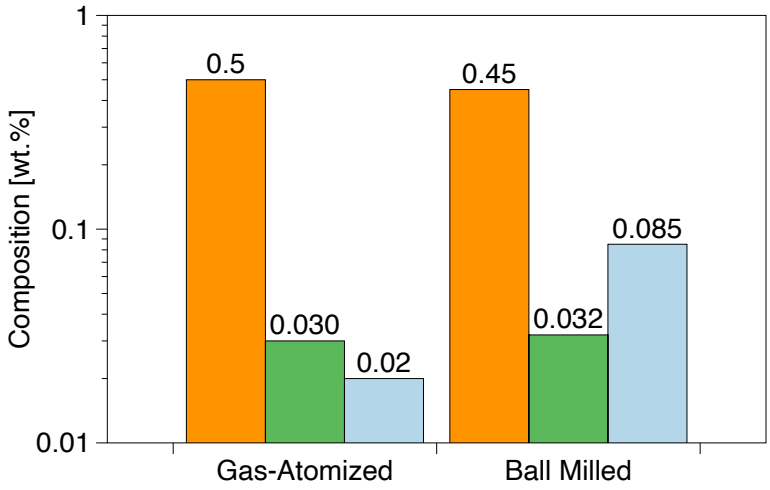

Figure 3. Chemical analysis of carbon (orange), nitrogen (green) and oxygen (gray) in the gas-atomized and ball-milled conditions.

Following mechanical alloying, 400 g of the NAFA-1 powder was packed into a mild steel can with a 2.9 in. outer diameter (OD). The powder was degassed at 300°C for 24 h prior to consolidation via extrusion at elevated temperature. For powder extrusion, the can was first heated to 850°C for 2 h to maximize nanoscale oxide precipitation. This was followed by an immediate subsequent anneal at 2 h at 1,000°C to allow for more effective powder consolidation. The ~3 in. OD can was then extruded through a rectangular die measuring 1.5 in. × 0.75 in. to produce the fully consolidated NAFA-1 alloy.

To have a reference material for comparison, the as-received gas-atomized VA05 powder was packed into a 3 in. thin-walled can and consolidated via hot-isostatic pressing (HIP). HIP consolidation performed at 150 Mpa during holding for 4 h at 1,050 °C. These parameters were chosen to promote densification without inducing significant grain growth beyond that of the initial powder grain size. In addition, the HIP treatment was also chosen so that the time and temperature experienced by the precursor powder (1,050 °C) would be similar to that of the NAFA-1 powder (1,000 °C) during consolidation.

In this report, the VA05 powder that was subjected to mechanical alloying and extrusion is designated (NAFA-1 because it is the first heat of the nanostructured AFAs being pursued in this work package. Conversely, the VA05 powder consolidated via HIP is aptly named HIP-AFA for comparison.

3. MICROSTRUCTURE AND MECHANICAL PROPERTIES OF HIP-AFA VS. NAFA-1

Microstructures of HIP-AFA and NAFA-1 were investigated using scanning electron microscopy (SEM) – energy dispersive x-ray spectroscopy (EDS). In addition, conventional transmission electron microscopy (TEM) and scanning transmission electron microscopy (STEM)-EDS was performed on the extruded NAFA-1 sample to investigate precipitate formation and to enable a comparison to the additively manufactured material later this year. SEM was performed using a MIRA 3 SEM by TESCAN USA, Inc., equipped with an Oxford Symmetry electron backscatter diffraction (EBSD) detector with a probe current of approximately 3 to 6 nA. All EBSD data were collected using a 20 kV accelerating voltage with a 6–8 nA beam current. The NAFA-1 specimen for TEM was prepared using a standard focused ion beam (FIB) process. Lift-out of a bulk sample with a length of 20 microns was subsequently thinned to a thickness of around 100 nm in the regions of interest. TEM was performed using an FEI (now Thermo Fisher Scientific, Waltham, MA, USA) Talos F200X operating at 200 kV. EDS was used to map element distributions across a field of view of 2,560 and 320 nm. Mappings were completed using a probe current of ~1 nA and a probe size of less than 1 nm with active drift correction every 10 s. The spectrum images were recorded using a pixel region of 1024 × 1024 with a 3 × 3 neighborhood averaging filter applied during image post-processing to increase signal. Scan duration for each map was approximately 1.5 hr. Figure 4 compares the grain structure and orientation in inverse pole figure (IPF) maps, kernel average misorientation (KAM) maps, and phase maps of HIP-AFA and NAFA-1. Grain dilation of up to 5 percent has been performed on EBSD maps in OIM software.

The IPF maps were evaluated top-to-bottom, which follows the extrusion direction of NAFA-1, resulting in a strong (001) texture and elongated grains. The kernel average misorientation maps do not show a significant difference, while the number density of the NiAl phase is significantly increased for NAFA-1. Differentiating between a NiAl and Fe-bcc phase is very challenging by only applying EBSD analysis, as the space group and lattice parameter of both phases are very similar with a Pm-3m and 0.2885 nm, and a Im-3m and 0.2849 nm, respectively. However, EDS analysis using STEM confirms the formation of a NiAl phase. The large difference in number density can only be explained by an extended annealing time for the NAFA-1 material below 900 °C during or after the hot-extrusion process in comparison with the HIP process used for the HIP-AFA material. Exposure at temperatures above of 900 °C completely dissolves NiAl and it would only form again during air-cooling according to the simulated phase composition shown in Figure 2. The area density of NiAl for HIP-AFA and NAFA-1 were calculated to be around 2.5 and 10.3 %, respectively. The grain size distribution of NAFA-1 is significantly reduced in comparison with the HIP-AFA material with an average area weighted grain diameter of the fcc matrix marked with red in Figure 4 of 1.4 ± 1.0 µm and 7.2 ± 2.8 µm, respectively. The NiAl phase marked with the color green in Figure 4 was investigated separately and is comparably in size for both materials with 0.52 ± 0.21 µm and 0.63 ± 0.22 µm for NAFA-1 and Hip-AFA, respectively.

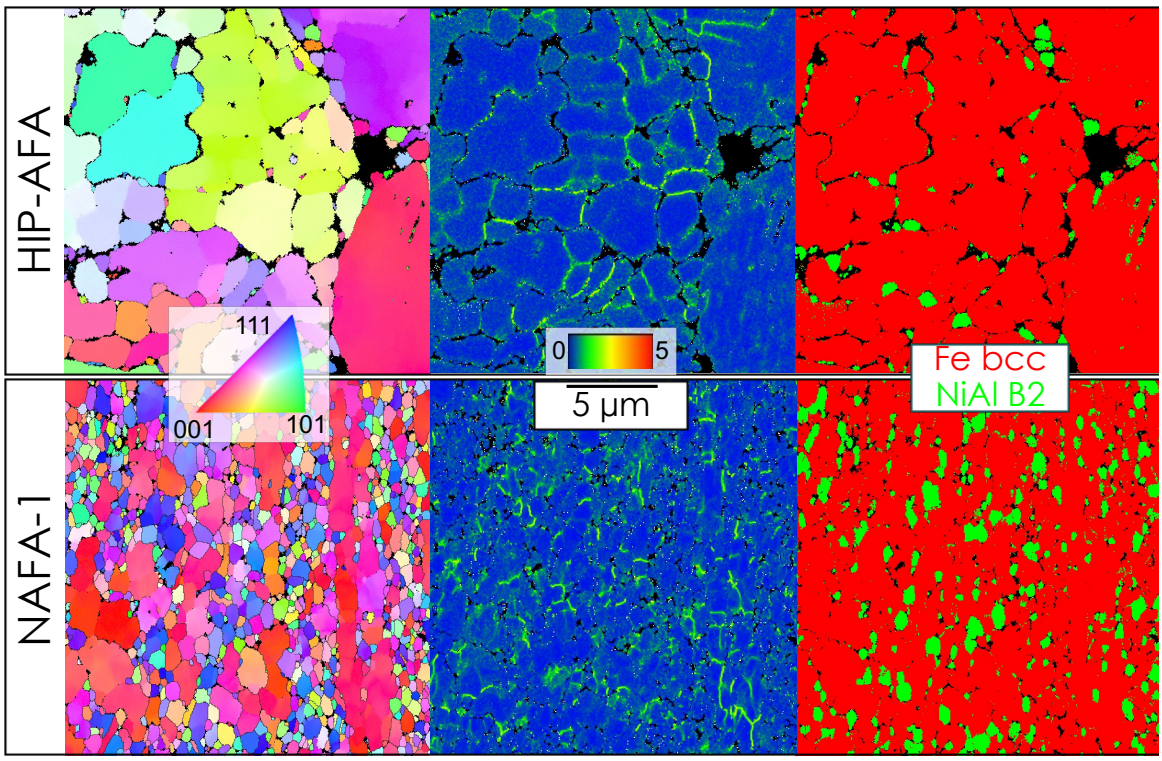

Figure 4. PF, KAM, and phase maps of HIP-AFA (top row) and NAFA-1 (bottom row). The IPF grain orientation is evaluated from top-to-bottom direction.

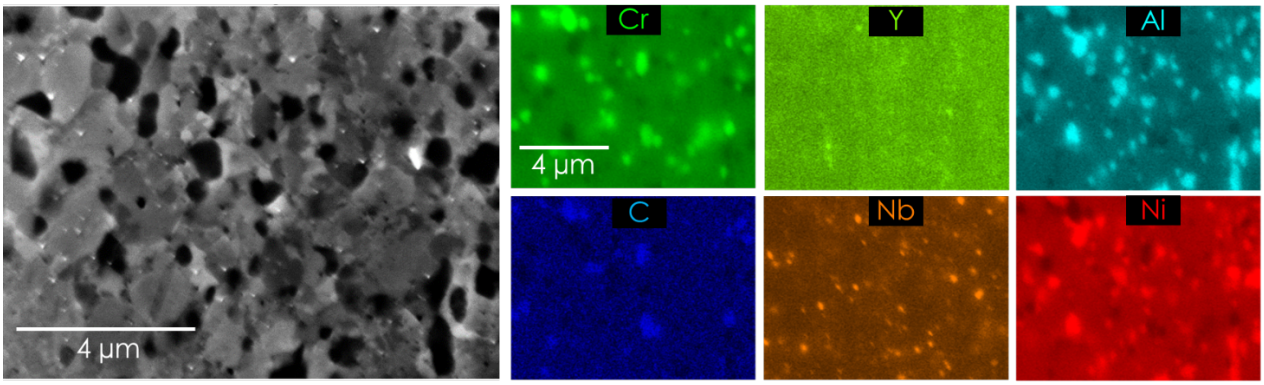

Figure 5. SEM back-scattered electron map of NAFA-1 and EDS maps of selected elements.

The SEM EDS maps of NAFA shown in Figure 5 exhibit Cr and C in similar locations compared to Al and Ni. Based solely on that analysis and the simulated phase composition map presented in Figure 2, it can be concluded that Cr-rich carbide phase, most likely $M_{23}C_6$ and Ni_xAl_y phases have formed. Nb cannot be associated to any other element in SEM EDS maps because the formed precipitates are relatively small for SEM resolution. The phase diagram in Figure 2 suggests a NbC formation, but an investigation method with a better resolution is required for confirmation. Yttrium was only visible in traces and was well distributed at SEM resolution and seemed to have formed small precipitates. Detailed microstructure characterization of nanosized precipitates formed during the mechanical alloying, and the subsequent extrusion process is of importance for this project. Therefore, STEM-EDS methods were employed. Figure 6 shows a bright field (BF) image of NAFA-1 with the STEM EDS map as an overlay of Ni (green), Y (pink), and Nb (blue). Those elements do not show up in the same locations, which highlights the different formed precipitates and intermetallic phases.

The grain boundaries are denuded of Ni, as Ni-rich precipitates have segregated by diffusion of Ni along the grain boundaries. Four areas representative of the major phases found (excluding carbon-rich precipitates) in the NAFA alloy were investigated, and the respective energy spectrum is shown in Figure 6. Area 1 highlights the yttrium-rich precipitates, which presents a mix of complex $Y_xAl_yO_z$ and Y_2O_3. Area 2 represents the matrix of the material as a reference, and area 3 shows the small Nb-rich precipitates, which could not be analyzed using SEM. STEM-EDS clearly shows the combination of Nb with C, as well as the addition of Zr. Area 4 displays the predicted NiAl phase.

Figure 7 presents an overview of all elemental maps in atomic percentage after an atomic number (ZAF) correction included in the Velox software. The Ni-denuded grain boundaries reveal an increase in Fe. Cr is mostly homogenously distributed but shows the formation of a carbide-rich phase at the bottom of the map, highlighted with a white arrow. The large $M_{23}C_6$ carbides visible in the SEM EDS maps were almost completely absent in the investigated TEM lamella, indicating that an investigation of a sample on multiple scales is necessary to understand the microstructure formation. Mo, W, Zr are co-located with NbC, whereas Y has formed several nanoscaled precipitates, as shown in the bottom of the Y map. The inhomogeneous distribution of yttrium-rich precipitates with several nanosized precipitates can be seen in the bottom half of the yttrium map in Figure 7, but there are almost no visible precipitates in the top half. This was further investigated using higher magnification. Figure 8 shows two regions in the BF image that were investigated using STEM EDS mapping. It is obvious that in the entire area, no yttrium-rich oxide has formed, but region B shows the small nanosized precipitates between some larger yttrium-rich precipitates in the 20 to 40 nm size range. Extended milling durations have been successful in forming a homogeneous distribution, but they also reduce economic viability for austenitic ODS steels.

X-ray diffraction (XRD) was performed on polished cross sectioned materials using 1D Bragg–Brentano (BB) geometry in a Rigaku SmartLab x-ray diffractometer equipped with a Cu Kα anode and a Cu Kβ filter. The goal was to determine if there is a difference in phase types between HIP-AFA and NAFA caused by mechanical alloying or processing. The XRD device used a HyPix-300 semiconductor detector with a 0.5° incident slit and a length-limiting slit of 5 mm. The first receiving slit was set to 3°, and the second receiving slit was fully open. The scan range was set to 20–120° for 2Theta,2θ with a fine step size of 0.01° and a scan speed of 1° per minute. The SmartLab Studio II software suite by Rigaku corporation was used for analysis of the data. Crystallographic structure information was imported from the Inorganic Crystal Structure Database (ICSD). Several ICSD codes—$M_{23}C_6$, Nb_2C, Ni_2Al_3, and Y_2O_3—were tried to match with the recorded patterns, but they did not line up with the measured lattice positions. The following phases showed a match and are discussed in detail below: Fe (ICSD collection code 185720) [4], NiAl (ICSD collection code 191110) [5], NbC (ICSD collection code 94449) [6], and Y (ICSD collection code 95176) [7].

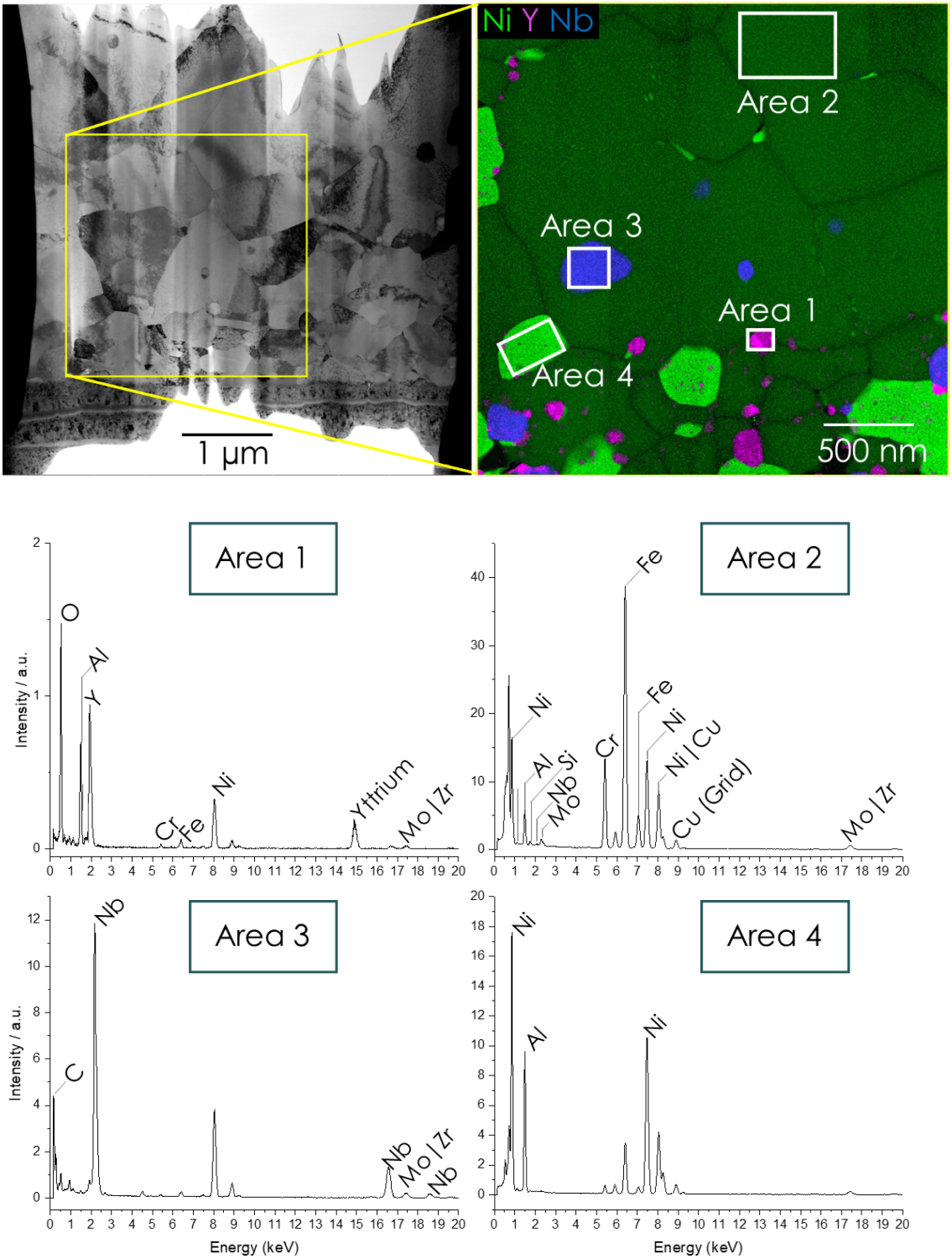

Figure 6. STEM BF image next to the EDS maps showing Ni, Y, and Nb. EDS spectra are extracted from four areas and are shown on the bottom.

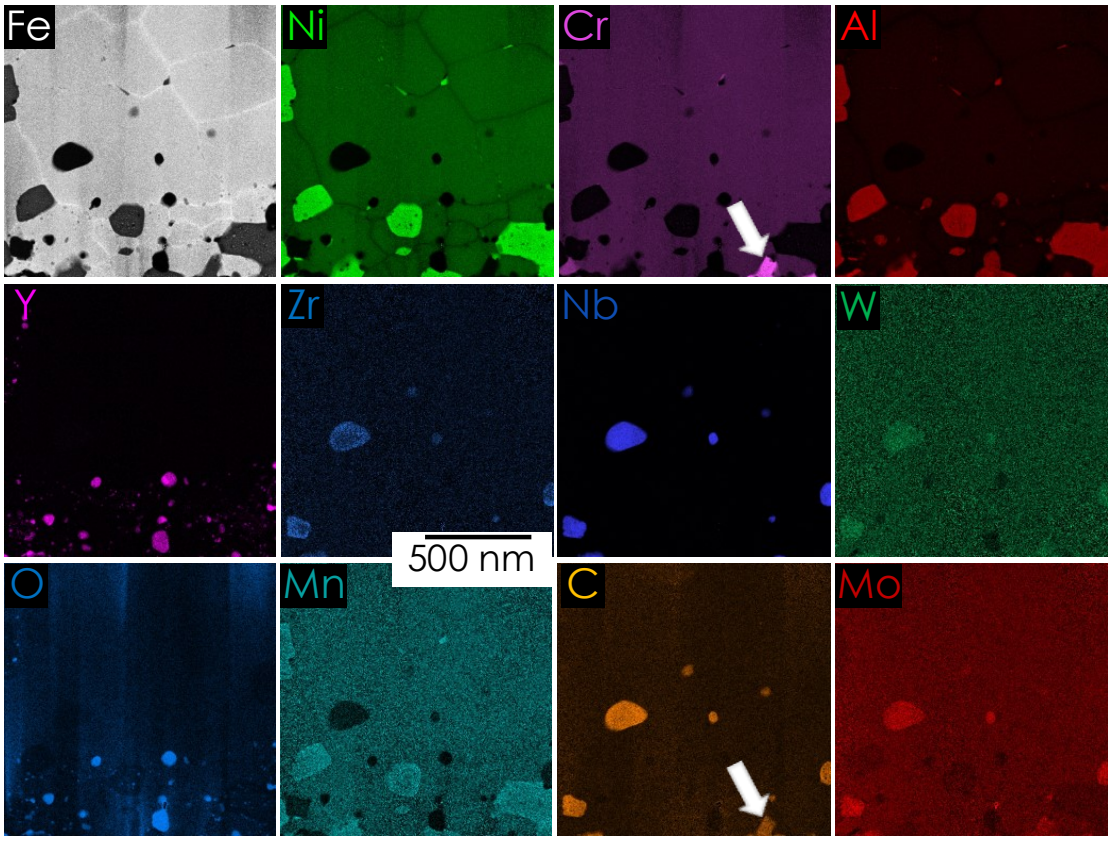

Figure 7. STEM EDS maps of all containing elements. The arrow is pointing at a Cr-rich $M_{23}C_6$ carbide.

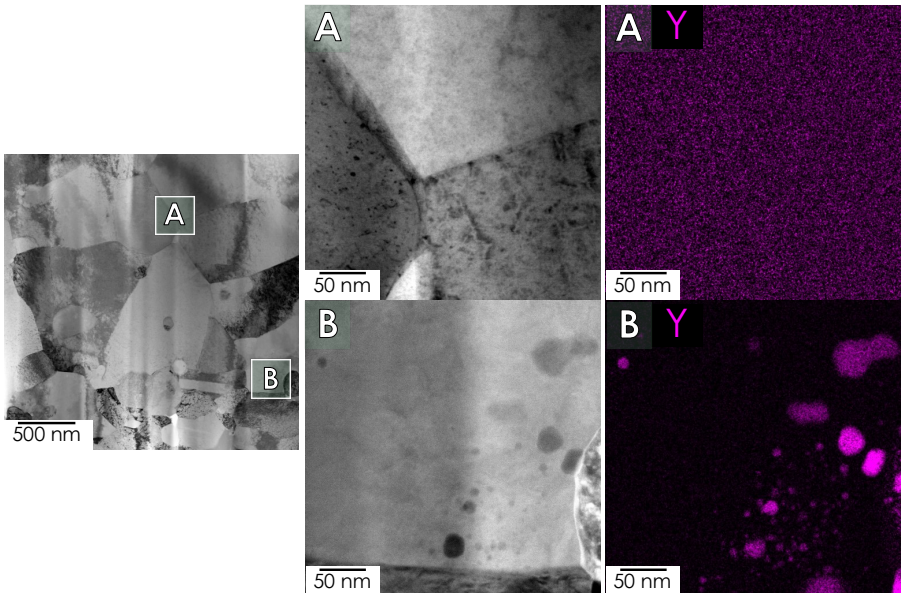

Figure 8. STEM BF map with two areas highlighting the heterogenous distribution of yttrium: no precipitates are shown in area A, but nanoscale yttrium-rich precipitates are visible in area B.

The resulting BB scans are shown in Figure 9 on an intensity log scale plotted against 2θ. The subject ICSD phase positions are shown below the BB scans. The differences between the HIP-AFA and NAFA-1 are marginal, with peak height discrepancies resulting from texture differences. The ratio between the (111) and (200) peaks at 42.9 and 50.0° for isotropic fcc Fe is approximately 1.6, with NAFA-1 showing a decreased ratio of 1.3 and a stronger (200) reflection because of the anisotropic texture in the extrusion direction.

The other difference between the two XRD spectra is the higher peak intensity for NAFA-1 at around 26.5° 2Theta, which corresponds2θ corresponding to an interplanar spacing of 0.34 nm. This interplanar spacing does not match any other intermetallic or carbide phase, but it lines up with the yttrium peaks (indicated by the green diamond symbol in Figure 9) in a non-oxidized state. A comparison of XRD and TEM results shows significant Y-rich precipitates, but those are sequestered with oxygen and sometimes form complex oxides with Al. Figure 7 shows that yttrium is clearly in an oxidized state, which makes the metallic yttrium peak unlikely. Even with the 0.3 wt.% added Y_2O_3 in NAFA-1, no Y_2O_3 was detectable using XRD methods. Those precipitates are not detectable in the recorded diffraction spectra because of the small size and quantity and/or volume fraction, in addition to a poor peak to background ratio, when using Cu Kα radiation on Fe-based materials due to the Fe K-radiation fluorescence. To exclude measuring errors causing the peak at 26.5° shown in XRD spectra, a second measurement was performed that showed the same results. It was found that the 0.34 nm interplanar spacing does not correspond with elements inside the sample; instead, it corresponds with the graphite resin used to embed the sample for polishing. That peak only showed up for the NAFA sample, because the sample size was much smaller than the HIP-AFA sample. Therefore, the peak at 26.5° is attributed to the used graphite resin. This demonstrates that a careful comprehensive analysis using TEM and XRD helped prevent misinterpretation of measured data.

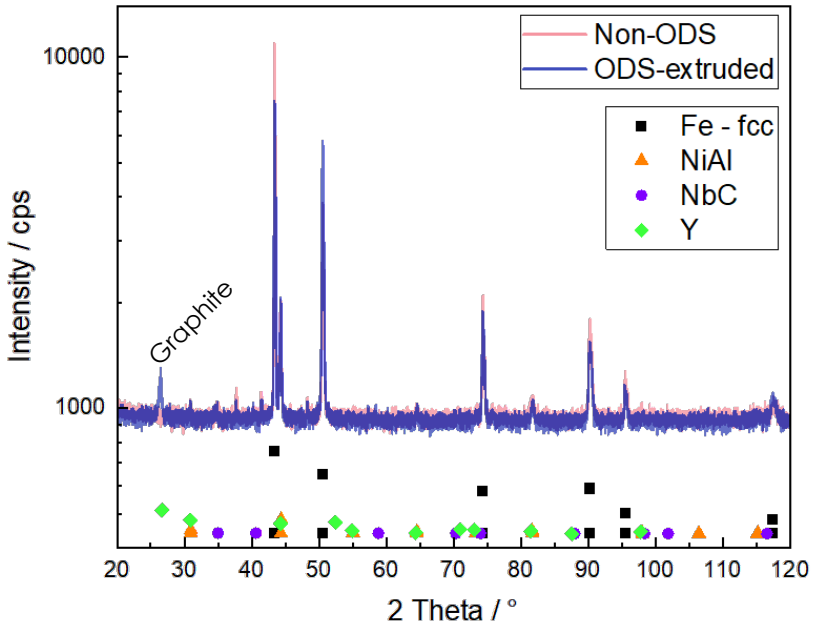

Figure 9. XRD BB scan from 20 to 120° for AFA and NAFA-1, with Bragg positions of four phases. The peak at 26.5° comes from the graphite-containing resin and provides a lesson-learned example.

Tensile tests from ambient atmosphere to temperatures of 800 °C were conducted for both the HIP-AFA and NAFA-1 materials. Tensile testing was conducted in air using an Instron mechanical test frame with a 5 kN load cell, with strain measured using crosshead displacement. Aside from the use of subsized specimens (SS-J2 geometry), care was taken to follow ASTM-E8/E21 standards for room temperature and elevated temperature tensile testing. The strain rate used for these tests was 10^{-3} s^{-1}. Only one sample was tested per temperature to screen mechanical properties. The results are shown in Figure 10 for HIP-AFA (red square) and NAFA-1 (blue triangle). Each symbol Yield stress (YS) and uniform elongation (UE) are represented by the solid symbols, and ultimate tensile stress (UTS) and total elongation (TE) are displayed with open symbols. The superior YS and UTS of NAFA-1 in comparison with HIP-AFA was expected because of the smaller grain size and pinning pressure of yttrium-rich precipitates. However, at increased temperatures between 400 and 600°C, a crossover of UT and YS is observed for HIP-AFA and NAFA-1.

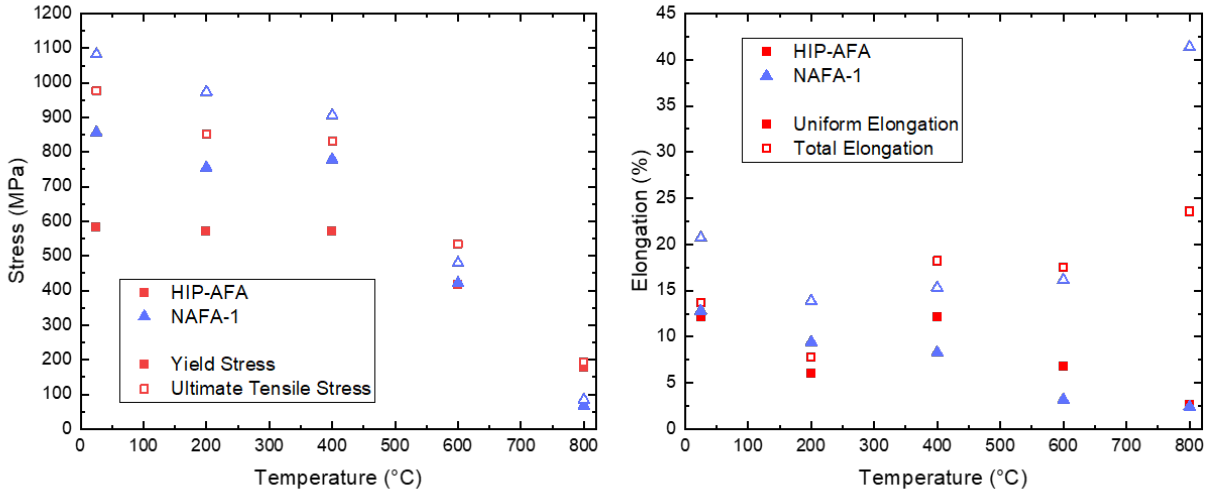

Figure 10. Tensile test results plotted for HIP-AFA and NAFA-1.

Multiple reasons can be found for this behavior: The much higher initial NiAl phase in NAFA-1 (10.3 % in comparison with 2.5%)—which%) impacts the high temperature properties of NAFA-1 negatively. NiAl is notorious for rapid loss of strength above temperatures of 550°C. Other contributing factors area slightly inhomogeneous distribution of nano-precipitates, the inability to suppress grain growth in certain grains, and a strong anisotropic texture—impacts the high-temperature properties of NAFA-1.. AFA steel'ssteels' high-temperature strength originates in precipitate strengthening from small carbides containing Nb, Mo, and Ti. However, with the weight percentages of those alloying elements comparably low and with carbon on the higher end, high-temperature strengthening was compromised. A clear indication that NAFA-1 has seen an extended heat treatment is shown in the increased total elongation compared with HIP-AFA, which usually occurs in aged AFA material [8]. Additionally, the mechanical alloying process of NAFA-1 steels must be optimized to achieve a better distribution of precipitates. However, it was necessary to select shorter mechanical alloying times with reduced revolutions per minute inside the mill needto preserve powder quantity. For future applications, austenitic matrix alloys. the mechanical alloying must be optimized, but another production route via additive manufacturing is beingwill be explored in an upcoming milestone.

4. A NEW POWDER COMPOSITION FOR A NEW NAFA PRODUCTION PROCESS

Additive manufacturing methods have been researched within the past decade to offer an alternative route for a scalable economically viable production of ODS steels. The goal is to address the issue of low number densities and growth of oxide precipitates during additive manufacturing [9]. Success of that research has been limited, failing to provide the required small precipitate sizes. Even though the required nanosized precipitates were producible using gas atomization reaction synthesis (GARS), the process could not produce high number densities of precipitates $>10^{22}$ m^{-3}. The powder manages to keep the oxide precipitate from forming rare earth elements in a metallic or intermetallic condition during gas atomization. The surface of the produced powder then becomes oxidized during additive manufacturing under an oxidizing environment (95% Ar + 5% O). This process has resulted in the desired sizes of oxide precipitates [9]. However, number densities remained one to three orders of magnitude below those of the conventionally manufactured ODS steels [10-12]. A high number of nanoscale precipitates is important to increase high-temperature creep performance; it acts as a sink for the irradiation induced defects and supports management of HTHE [13-15].

An increase of rare earth elements using the GARS process did not result in an increased number density of precipitates. Instead, agglomeration of yttrium inside the gas-atomized powder led to an unacceptable increase in nanoprecipitate sizes. To overcome the issue of a low number density of precipitates while keeping the size of oxide precipitates in the intended range of 2 to 20 nm, a second phase of precipitates must be sequestered, and the sink strength must be increased. To achieve this, the pre-alloy composition needed to be changed to enable the formation of a second phase precipitate. Elements capable of forming small-scaled precipitates which do not interfere with the oxide precipitate formation were evaluated, and the composition was adjusted to reflect that the findings. Nitrides were chosen as the preferred precipitates, with Zr as the major element to react with nitrogen. Nb has been increased to capture carbon and to help with oxidation resistance of the matrix, thus improving creep-rupture life. Printing will be performed under a nitrogen-containing atmosphere, with 5 percent oxygen to foster ODS precipitate formation while enabling formation of nitrides as a second phase. The nitrogen content will be varied, and nitride-forming element contents are increased in the new NAFA-2 alloy. The final composition for a new NAFA alloy is shown in Table 2..Table 2, as taken from supplier documentation. The Cr content was decreased to avoid sigma phase formation, and Ni was increased to address the reduced carbon content. Carbon content was reduced to decrease the amount of large $M_{23}C_6$, because those precipitates tend to grow rapidly during annealing and operating conditions. The content of Mo was increased as a solution-strengthening element, and tungsten was removed. Mn was reduced to a minimum because it can compromise the continuous alumina scale. The resulting phase diagram is presented in Figure 11Figure 11 without showing the impacts from the GARS process and the addition of nitrogen and oxygen to form precipitates.

Table 2. Specified chemical compositions of INM-specific gas-atomized AFA powder used for future work.
Compositions are in weight percent as provided in supplier material certifications.

Element	NAFA-2			
	Target (wt %)	Target Min (wt %)	Target Max (wt %)	Measured (wt.%)
Fe	**Bal.**	Bal.	Bal.	Bal.
Cr	15	14.5	15.5	15.17
Mn	0.2	0.1	0.3	0.25
Ni	25	24.5	25.5	25.31
Cu	-	-	0.1	0.009
Al	3.75	3.5	4	3.58
Si	0.2	0.1	0.3	0.2
Nb	1.5	1.3	1.7	1.37
Mo	2	1.8	2.2	1.98
W	-	-	0.1	0.004
V	-	-	0.05	0.001
Ti	-	-	0.05	0.031
Zr	0.18	0.16	0.2	0.21
C	-	-	0.05	0.007
B	-	-	0.01	<0.001
N	-	-	0.03	0.029
Y	0.13	0.13	0.17	0.13

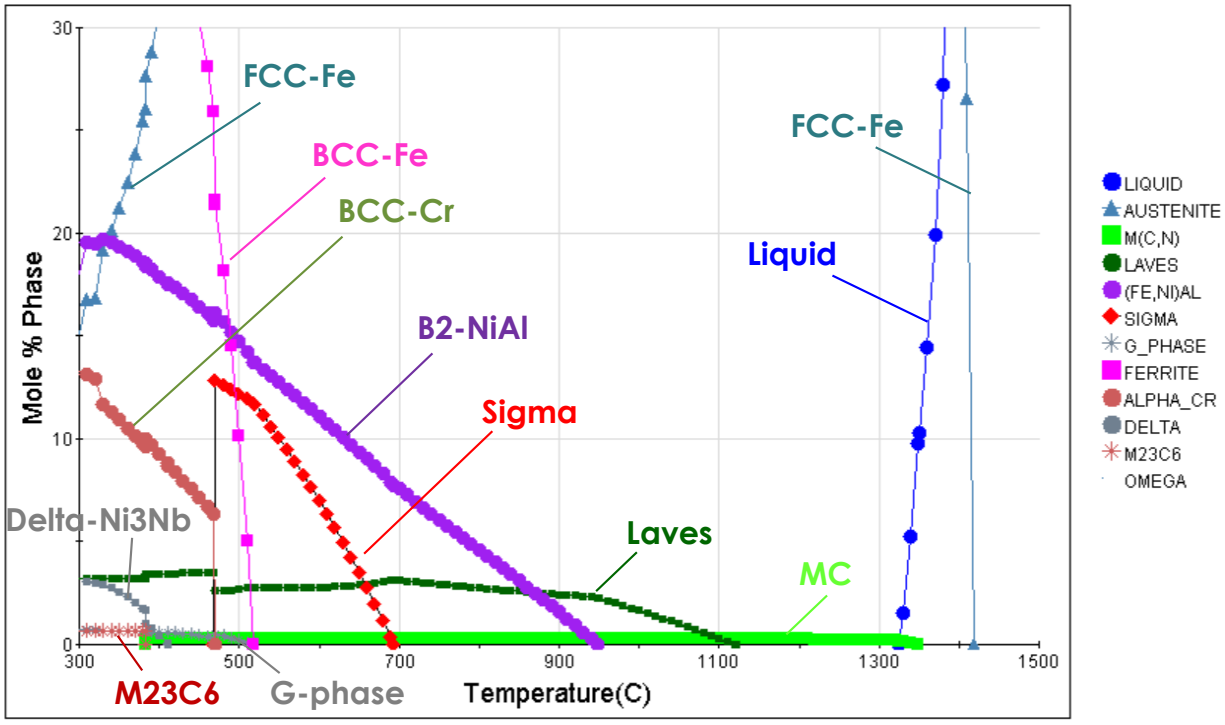

Figure 11. Phase diagrams for new NAFA-2 gas atomized powder.

5. CONCLUSIONS

Two AFA steels were produced as references for the optimized NAFA-2 steel. The HIP-AFA was produced directly from the gas-atomized powder, and the NAFA-1 variant used the same pre-alloy but was mechanically alloyed to form nano-sized precipitates. Mechanical alloying of the AFA powder resulted in a reduced yield, but microstructure characterization was able to identify inhomogenously distributed nanosized precipitates. Nevertheless, the formation of such small nanoprecipitates for the reduced milling conditions and a strong increase in yield strength and elongation up to 550° is positively remarkable. Mechanical alloying resulted in an oxygen pickup 3 times the amount found in the gas-atomized powder, which is mostly attributed to the addition of Y_2O_3 to the material. The grain size in NAFA-1 was smaller in comparison with HIP-AFA in its as-produced condition, resulting in superior mechanical properties. However, the high temperature properties above 550° dropped significantly, which is typical for a material with a large amount of NiAl phase. This behavior leaves room for the optimization of the NAFA-1 composition that was performed in this study. The NAFA-2 alloy composition was selected and will be used with a novel processing route implementing additive manufacturing processes to overcome the economically nonviable route of mechanical alloying while producing a dual-precipitation–strengthened AFA steel. The new material should show improved high-temperature properties in comparison with NAFA-1 and should also produce nanoprecipitates in a scalable way. These results would open up a new route to increase nanoprecipitate AFA steels for industry-scale production.

6. REFERENCES

[1] Y. Yamamoto, M.P. Brady, Z.P. Lu, P.J. Maziasz, C.T. Liu, B.A. Pint, K.L. More, H. Meyer, E.A. Payzant, Creep-resistant, Al2O3-forming austenitic stainless steels, Science 316(5823) (2007) 433-436.
[2] B.A. Pint, Y.-F. Su, M.P. Brady, Y. Yamamoto, J. Jun, M.R. Ickes, Compatibility of Alumina-Forming Austenitic Steels in Static and Flowing Pb, Jom 73(12) (2021) 4016-4022.
[3] C. Massey, D.T. Hoelzer, Y. Yamamoto, T.G. Seibert, S. Dryepondt, H. Hyer, J. Kendall, M. Zach, Progress on Design and Production of Oxide Dispersion–Strengthened Alumina-Forming Austenitic Alloys for Nuclear Applications, Oak Ridge National Laboratory (ORNL), Oak Ridge, TN (United States), 2023.
[4] Y. Nishihara, Y. Nakajima, A. Akashi, N. Tsujino, E. Takahashi, K.-i. Funakoshi, Y. Higo, Isothermal compression of face-centered cubic iron, American Mineralogist 97(8-9) (2012) 1417-1420.
[5] N. Belyavina, V. Markiv, O. Nakonechna, F. Lozovyi, Phase equilibria in the Ni–Al–Ga system at 700° C, Journal of alloys and compounds 593 (2014) 41-49.
[6] G. Will, R. Platzbecker, Crystal structure and electron density distribution in niobium carbide, Zeitschrift für anorganische und allgemeine Chemie 627(9) (2001) 2207-2210.
[7] R.O. Demchyna, S.I. Chykhrij, Y.B. Kuz'ma, Y–Cu–P system, Journal of Alloys and Compounds 345(1) (2002) 170-174.
[8] L. Liu, C. Fan, H. Sun, F. Chen, J. Guo, T. Huang, Research Progress of Alumina-Forming Austenitic Stainless Steels: A Review, Materials (Basel) 15(10) (2022).
[9] T. Horn, C. Rock, D. Kaoumi, I. Anderson, E. White, T. Prost, J. Rieken, S. Saptarshi, R. Schoell, M. DeJong, Laser powder bed fusion additive manufacturing of oxide dispersion strengthened steel using gas atomized reaction synthesis powder, Materials & Design 216 (2022) 110574.
[10] L. Autones, P. Aubry, J. Ribis, H. Leguy, A. Legris, Y. de Carlan, Assessment of Ferritic ODS Steels Obtained by Laser Additive Manufacturing, Materials 16(6) (2023) 2397.
[11] S. Saptarshi, M. DeJong, C. Rock, I. Anderson, R. Napolitano, J. Forrester, S. Lapidus, D. Kaoumi, T. Horn, Laser Powder Bed Fusion of ODS 14YWT from Gas Atomization Reaction Synthesis Precursor Powders, JOM 74(9) (2022) 3303-3315.
[12] H. Jia, Z. Zhou, S. Li, A new strategy for additive manufacturing ODS steel using Y-containing gas atomized powder, Materials Characterization 187 (2022) 111876.
[13] T. Gräning, M. Rieth, J. Hoffmann, A. Möslang, Production, microstructure and mechanical properties of two different austenitic ODS steels, Journal of nuclear materials 487 (2017) 348-361.
[14] J. Chen, P. Jung, T. Rebac, F. Duval, T. Sauvage, Y. De Carlan, M. Barthe, Helium effects on creep properties of Fe–14CrWTi ODS steel at 650° C, Journal of Nuclear Materials 453(1-3) (2014) 253-258.
[15] P. Edmondson, C. Parish, Q. Li, M. Miller, Thermal stability of nanoscale helium bubbles in a 14YWT nanostructured ferritic alloy, Journal of nuclear materials 445(1-3) (2014) 84-90.